

ORIGINAL ARTICLE

Van der Waals epitaxy between the highly lattice mismatched Cu-doped FeSe and Bi₂Te₃

Arsham Ghasemi¹, Demie Kepaptsoglou², Pedro L Galindo³, Quentin M Ramasse², Thorsten Hesjedal⁴ and Vlado K Lazarov¹

We present a structural and density functional theory study of Fe_xCu_{1-x}Se within the three-dimensional topological insulator Bi₂Te₃. The Fe_xCu_{1-x}Se inclusions are single-crystalline and epitaxially oriented with respect to the Bi₂Te₃ thin film. Aberration-corrected scanning transmission electron microscopy and electron energy loss spectroscopy show an atomically sharp Fe_xCu_{1-x}Se/Bi₂Te₃ interface. The Fe_xCu_{1-x}Se/Bi₂Te₃ interface is determined by Se–Te bonds and no misfit dislocations are observed, despite the different lattice symmetries and large lattice mismatch of ~19%. First-principle calculations show that the large strain at the Fe_xCu_{1-x}Se/Bi₂Te₃ interface can be accommodated by van der Waals-like bonding between Se and Te atoms. *NPG Asia Materials* (2017) 9, e402; doi:10.1038/am.2017.111; published online 7 July 2017

INTRODUCTION

Heterostructured materials are the basis of metal–oxide–semiconductor transistor and data storage technologies. Besides the tremendous importance of multi-layered thin films for device applications, heterostructured interfaces have also been for the past decades a playground for the discovery of novel physical phenomena, e.g., the quantum Hall effect.¹ One of the main criteria for realising new, interface-related heterostructure behaviours is the ability to control the atomic and electronic properties on an atomic level. This typically requires creating epitaxially matched superlattices. One of the main challenges in creating such superlattices is the lattice mismatch between the individual single crystal components.^{2,3} Having different symmetries and lattice parameters lead to built-in strain in the interface region,⁴ which ultimately changes the electronic properties of the system.⁵ Due to the strong chemical bonds between the atomic layers at the heterostructure interface, this effect already occurs at very low values of the lattice mismatch.

In contrast to strongly bonded heterointerfaces, epitaxial heterostructures can also be realised by weak van der Waals (vdW) interactions,⁶ as demonstrated for heterostructures comprising, e.g., 2D materials, graphene, boron nitride and transition metal dichalcogenides^{7–9} and layered materials such as Bi₂Se₃ and Bi₂Te₃.^{10,11} Here, despite the constraints such as large lattice mismatch (up to 19%) and different crystallographic orientations, novel heterostructures can be realised, using these layers as Lego-like building blocks, allowing for the design of atomically thin electronic device materials with outstanding properties.⁸

Heterointerfaces have recently also attracted attention as a platform for realizing exotic quantum phenomena, e.g., by combining a superconductor with a topological insulator.^{12–17} Proximity effects in this type of interface are predicted to give rise to so-called Majorana

fermions.^{13,18,19} Experimentally, the proximity effect at the superconductor/topological insulator interface has been investigated in FeTe/Bi₂Te₃ heterostructures,^{15,17,18,20,21} and induced superconductivity in the topological insulator has been observed with a transition temperature (T_c) of around 12 K.¹⁵ Due to the much higher T_c of Cu-based superconductors, other candidates for these heterostructures include CuSe and Cu-doped FeSe and FeTe.²² The main issues in fabricating such heterostructures are the different crystallographic structure, FeSe has tetragonal structure (P 4/nmmS) and Bi₂Te₃ has trigonal structure ($R\bar{3}m$), and the very large lattice mismatch of 19%.

In this work, we demonstrate that single-crystalline, misfit-dislocation free interfaces between tetragonal Cu-doped FeSe and trigonal Bi₂Te₃ symmetry lattices with very large lattice mismatch (19%) can be realised, using scanning transmission electron microscopy (STEM) and electron energy loss spectroscopy (EELS). Large inclusions of Fe_xCu_{1-x}Se are fully epitaxially embedded in the Bi₂Te₃ film-matrix. We show that the calculated strain energy associated with the large mismatch is rather small; hence no misfit lattice dislocations are formed. An atomically resolved interface structure analysis of Fe_xCu_{1-x}Se/Bi₂Te₃ shows that the Se and Te atomic columns are relaxed in-plane, so the overall strain is less than 10%. According to density functional theory (DFT) total energy calculations, the energy cost associated with such displacements of the atomic columns is less than 0.01 eV, which is significantly lower than the thermal energy at room temperature (0.0257 eV).

MATERIALS AND METHODS

The Bi₂Te₃ thin films were grown by molecular beam epitaxy (MBE) on *c*-plane sapphire substrates using a growth protocol described in detail in ref. 23 Bi, Fe, Cu and Te were evaporated from standard effusion cells, whereas Se was supplied out of a cracker cell. All elements were of 99.9999% purity. Their flux

¹Department of Physics, University of York, York, UK; ²SuperSTEM Laboratory, SciTech Daresbury Campus, Daresbury, UK; ³Department of Computer Science and Engineering, Universidad de Cádiz, Puerto Real, Spain and ⁴Department of Physics, Clarendon Laboratory, University of Oxford, Oxford, UK
Correspondence: Dr VK Lazarov, Department of Physics, University of York, York YO10 5DD, UK.
E-mail: Vlado.lazarov@york.ac.uk

Received 7 March 2017; revised 5 May 2017; accepted 8 May 2017

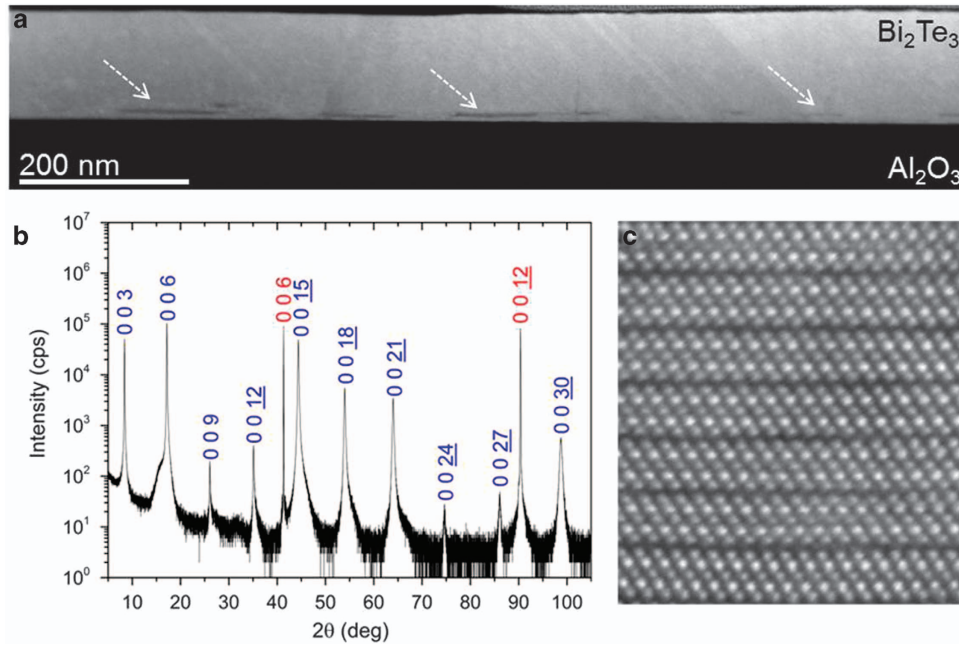


Figure 1 HAADF-STEM image and X-ray diffraction spectrum of Fe_xCu_{1-x}Se inclusions in the Bi₂Te₃ film on the Al₂O₃ substrate. (a) Low-magnification HAADF-STEM image of the Bi₂Te₃ film on the Al₂O₃ substrate; the dashed arrows outline the Fe_xCu_{1-x}Se inclusions in the Bi₂Te₃ film; (b) X-ray diffraction spectrum showing both Al₂O₃ substrate (red labels) and Bi₂Te₃ film peaks (blue labels); (c) atomically resolved HAADF-STEM image shows the quintuple layer structure of the Bi₂Te₃ film.

was monitored using a beam-flux monitor. The base pressure of the growth chamber was 1×10^{-10} Torr. The X-ray diffraction (XRD) measurements were carried out on a Rigaku Smartlab diffractometer using a rotating Cu anode (incident Cu K- α_1 radiation) in the standard Bragg–Brentano geometry.

Cross-sectional transmission electron microscopy (TEM) specimen preparation was carried out by focused ion beam (FIB) using a FEI Nova 200 NanoLab instrument. First a ~ 10 -nm-thick layer of carbon was thermally evaporated onto the film surface outside of the FIB chamber to reduce possible charging effects, as well as protecting the surface from damage. Before starting the milling procedure in the FIB, a ~ 500 -nm-thick Pt sacrificial layer was deposited using the electron beam to protect the film from Ga-ion implantation, followed by a ~ 3 - μm -thick Pt layer using the Ga beam to further protect the surface from any implantations and damage during the FIB process. For milling the trenches on both sides of the Pt-deposited area, we first tilted the stage $\pm 2^\circ$ from the position in which the Ga beam is perpendicular to the surface (52°), and then used an ion beam at 30 kV acceleration voltage and 6.5 nA beam current to mill the material out. In order to thin down the sample to the thickness required for 100 kV STEM imaging, after attaching the lamella to the Cu grid, we used a four steps procedure. First, we tilted the lamella by $\pm 2^\circ$ and used a 16 kV beam with 0.47 nA, then tilted $\pm 1.5^\circ$ and used a 16 kV beam, with 0.13 nA and 45 pA. After that, we tilted the specimen for $\pm 1^\circ$ and used a current of 21 pA. For the last thinning step, we tilted the lamella by $\pm 0.5^\circ$ and used 5 kV and 16 pA as beam parameters. When the sample approximately reached the required thickness, we performed a cleaning step by tilting the lamella by 45° and using a 2 kV Ga beam with 10 pA of current.

STEM imaging and EELS measurements were performed in a Nion UltraSTEM100 equipped with a Gatan Enfina spectrometer. The microscope was operated at 100 kV, with a convergence angle of 30 mrad; in these optical conditions the electron probe size is estimated to be ~ 0.9 Å. The inner detector angle for high-angle annular dark field (HAADF)-STEM imaging was 76 mrad. The native energy spread of the electron beam for EELS measurements was 0.3 eV, with the spectrometer dispersion set at 1 eV/channel. The EELS collection angle was 33 mrad. For enhancing the contrast of the atomically resolved spectra, a noise-reduction routine was applied using principal component analysis (CiMe- plugin for Gatan's Digital Micrograph 2.3 software suite).²⁴

Structure optimisation, total energy and electronic-structure calculations were performed from first-principles using the plane-wave DFT program CASTEP²⁵ with the generalised gradient approximation (GGA) of Perdew-Burke-Ernzerhof (PBE)²⁶ for the exchange-correlation functional. Ultrasoft pseudopotentials were used for each element, with 600 eV plane-wave cutoff energy for FeSe and FeTe formation energy calculations. Furthermore, a 500 eV plane-wave cutoff energy has been used for the Se bonding energy calculations to investigate the bonding nature of Se atoms in various positions on top of the Bi₂Te₃. Internal atomic positions were fully optimised until the force on each atom is ≤ 0.05 eV Å⁻¹ and the total energy converges within 0.02 meV/atom. The Brillouin zone was sampled using a Monkhorst-Pack²⁷ k-mesh of $6 \times 6 \times 6$, $5 \times 5 \times 5$, $7 \times 7 \times 7$, $6 \times 6 \times 4$, $9 \times 9 \times 6$ and $5 \times 5 \times 1$ for bulk Fe, Se, Te, FeSe, FeTe and Bi₂Te₃, respectively. Trigonal and tetragonal lattice constants for bulk Bi₂Te₃ ($a = 4.43$ Å and $c = 30.53$ Å) and FeSe ($a = b = 3.68$ Å and $c = 5.03$ Å) were also calculated from first-principles. A semi-empirical dispersion correction²⁸ is included to account for the weak vdW interactions, as well as a 30 Å-thick space of vacuum on top of the Se atom in the bonding energy calculations.

RESULTS AND DISCUSSION

Figure 1a shows a cross-sectional HAADF-STEM overview of the Bi₂Te₃ thin film grown on *c*-plane Al₂O₃ by MBE. Due to the atomic number dependence of the HAADF imaging ($\sim Z^{1.8}$), the Bi₂Te₃ film is clearly outlined with respect to the Al₂O₃ substrate. The film has a uniform thickness of 120 nm and a flat surface morphology. The XRD results further shows the single-crystalline nature of the grown film on a larger length scale (Figure 1b). The observed family of (003) peaks are representative of the rhombohedral symmetry class of Bi₂Te₃ ($R\bar{3}m$). Note, however, that the occurrence of the (0 0 9), (0 0 12) and (0 0 24) peaks is characteristic of unit cells distortions, e.g., due to doping.^{29,30} Atomic-resolution HAADF imaging (Figure 1c) shows the distinctive Te-Bi-Te-Bi-Te quintuple layer repeat unit of the Bi₂Te₃ film. The lower intensity regions, close to the interface, correspond to Fe_xCu_{1-x}Se inclusions, as outlined with dashed arrows in Figure 1a.

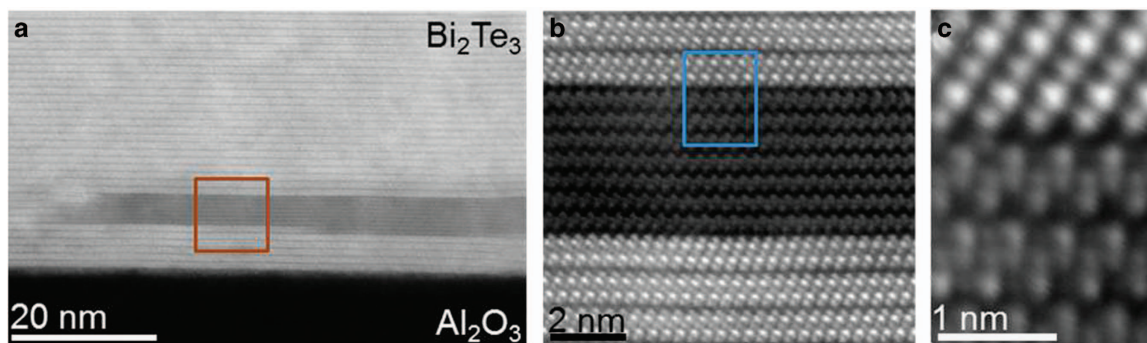


Figure 2 Higher magnifications HAADF-STEM image of Fe_xCu_{1-x}Se inclusions in the Bi₂Te₃ film. (a) Overview image of the Fe_xCu_{1-x}Se inclusion close to the Bi₂Te₃/Al₂O₃ interface; (b) magnified HAADF-STEM image from the region of interest outlined in (a); both the film and the Fe_xCu_{1-x}Se inclusion show good crystallinity; (c) high-magnification HAADF-STEM image from the interfacial region between the Bi₂Te₃ film and the Fe_xCu_{1-x}Se outlined in (b).

In order to reveal the atomic structure of the Fe_xCu_{1-x}Se phase, and the ordering at the Fe_xCu_{1-x}Se/Bi₂Te₃ interface, we performed atomically resolved HAADF-STEM imaging. Figure 2 shows a typical region of Fe_xCu_{1-x}Se/Bi₂Te₃ acquired in a [11 $\bar{2}$ 0] zone axis. Figure 2a shows details of the interfacial region containing the Fe_xCu_{1-x}Se inclusion. Higher magnification HAADF-STEM images from the regions outlined in Figure 2a and b show the atomic stacking of Fe_xCu_{1-x}Se, as well as the interface between Fe_xCu_{1-x}Se and Bi₂Te₃ (Figure 2b and c). The Fe_xCu_{1-x}Se inclusion is crystalline, with an atomically sharp interface with the Bi₂Te₃ film. Based on the atomic column Z-dependent contrast, the identification of the atomic structure at the interface can be carried out. The large difference between the atomic number of Bi and Te enables an easy differentiation between Bi and Te atomic columns. Similarly, the difference between the Cu and Se columns can be established, even though the intensity change is much smaller due to low difference in Z (Figure 2c). The HAADF intensities indicate that the bonding across the interface consists of Se–Te bonds.

Next, we present the chemical structure analysis of the inclusions and the interface between Fe_xCu_{1-x}Se/Bi₂Te₃ by EELS elemental mapping. Figure 3a shows a HAADF-STEM survey image from the Fe_xCu_{1-x}Se/Bi₂Te₃ interfacial area selected for chemical mapping. Figure 3b shows the HAADF-STEM image from the region of interest outlined in Figure 3a which is simultaneously acquired with the EELS elemental maps for Te, Fe, Cu and Se (Figure 3c–f). The L_{2,3} edges were used to map Fe, Cu and Se, and M_{4,5} for mapping Te. The chemical maps confirm the suggestion from HAADF imaging that the inclusion consists of Fe, Cu and Se (Figure 3d–f). Since both FeSe and CuSe share the same structure, and Cu and Fe have similar size, Cu can easily substitute Fe within the tetragonal inclusion structure, as indicated in the Figure 3d and e. The relative amount of Cu within FeSe inclusions is within 25 ± 10% range, varying spatially among the inclusions. We note that Fe is continuously evaporated during the Bi₂Te₃ growth, hence outside the inclusion acts as a dopant for Bi₂Te₃ film.³¹ The Se–Te atomic structure of the inclusion film interface is further supported by the EELS mapping from interface region shown in Supplementary Figure S1.

We also would like to note that the tetragonal phase of the inclusions is due to FeSe since the CuSe lowest structural phase is the hexagonal phase in comparison to tetragonal and orthorhombic phases.^{32,33} HAADF-STEM image simulations clearly show the tetragonal structure of the inclusions (Supplementary Figure S2). Furthermore DFT calculations prove that in an environment in which both Se and Te atoms are present, the formation of FeSe is more favourable than FeTe by ~ 0.78 eV/formula unit.

The atomic resolution images of the interface further help identify the crystallographic orientation between Fe_xCu_{1-x}Se and Bi₂Te₃ as: Fe_xCu_{1-x}Se(100)∥Bi₂Te₃(11 $\bar{2}$ 0) and Fe_xCu_{1-x}Se(001)∥Bi₂Te₃(0001). Bearing in mind the different crystallographic structures of Fe_xCu_{1-x}Se and Bi₂Te₃, as well as their lattice mismatch of 19%, one should expect a significant strain to develop at the Fe_xCu_{1-x}Se/Bi₂Te₃ interface. However, as shown next, no misfit dislocation are found at the interface indicating that the bonding between tetragonal Fe_xCu_{1-x}Se and trigonal Bi₂Te₃ is rather weak, i.e., vdW-like. Figure 4a shows a top view model of the interfacial Te and Se atomic planes. The positions of the first Se layer are shown with blue rectangles on top of the red Te atoms. For clarity, the cross-sectional view of these two layers is also shown. The geometrical matching between the two lattices, e.g., along the [10 $\bar{1}$ 0] direction, shows that the coincidental lattice spots appear for every fifth Te atom, i.e., every sixth Se atom, which gives ~ 19% mismatch of the lattices. The realisation of such a structure is strongly unfavourable due to very large strain at the interface. Hence the formation of misfit dislocations is generally the mechanism that governs either covalently or ionically bonded heterostructures. However, a misfit-dislocation network is not observed in our HAADF images. By using the atomic resolution images of the interface, we calculate the atomic column displacement of the Se and Te interface columns with respect to the columns away from the interface region, to which we refer as ‘bulk’ columns. Figure 4b shows the variation of the interfacial atomic column positions with respect to the bulk for both Se and Te. The data shows the absence of the periodic interface atomic displacement (present when dislocation network forms), and arbitrary (random-like) variation with respect to the average bulk Se/Te atomic columns distances, with Se atomic columns having slightly larger displacements compared to Te. This implies that the bonding between the Fe_xCu_{1-x}Se and Bi₂Te₃ is rather weak.

In order to gain insight into the nature of the bonding between the Fe_xCu_{1-x}Se and Bi₂Te₃ layers, we performed first-principle calculations. Since the interface bonding is mostly determined by the bonding between the first neighbouring atomic planes, we focused the analysis on calculating the bonding energy of the Se atom with respect to high symmetric points of the Bi₂Te₃ unit cell, i.e., the so-called top, bridge and hollow sites, respectively. In addition to these high symmetric points, we also calculated the bonding energy at positions in-between them along the main paths within the unit cell, e.g., [10 $\bar{1}$ 0], [11 $\bar{2}$ 0] and [01 $\bar{1}$ 0] (Figure 5a). In total we performed energy calculations for 32 distinct configurations, in which Se is displaced by ~ 0.1 Å along the calculated paths. Figure 5b gives a summary of the results, where representative configurations of the Se–Bi₂Te₃ unit cell are shown. First, it is worth noting that the energy only changes by a

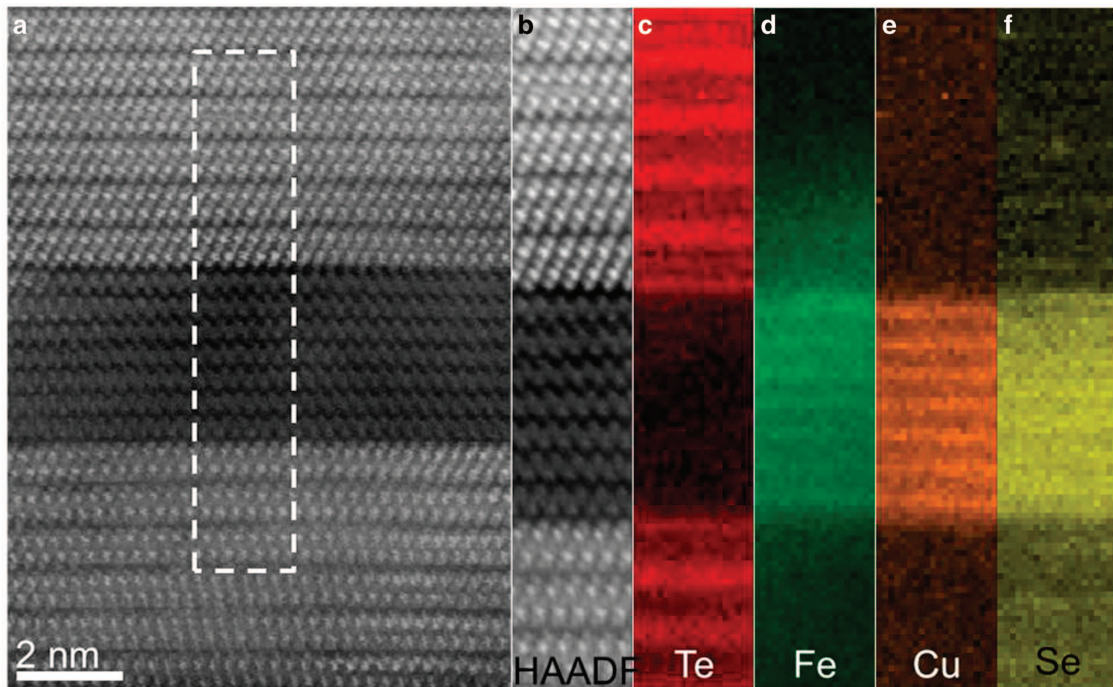


Figure 3 EELS elemental mapping of Fe_xCu_{1-x}Se inclusions and the Bi₂Te₃ film. (a) HAADF-STEM survey image from the Bi₂Te₃ film and the Fe_xCu_{1-x}Se inclusion. (b) HAADF-STEM signal from the region outlined by a dashed rectangle in (a), obtained simultaneously with the EELS data; (c–f) show Te *M*_{4,5}, Fe *L*_{2,3}, Cu *L*_{2,3} and Se *L*_{2,3} EELS signals at the Fe_xCu_{1-x}Se/Bi₂Te₃ interface, respectively.

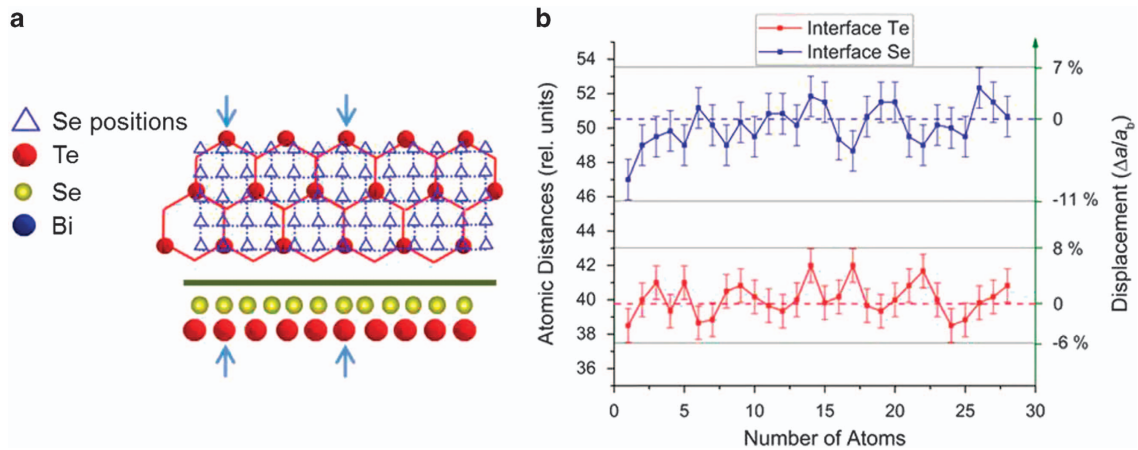


Figure 4 Schematic position and measured displacement of the Se and Te atoms at the interface between the Fe_xCu_{1-x}Se inclusions and the Bi₂Te₃ film. (a) Top view model of the Bi₂Te₃ lattice shows the trigonal crystal structure of the film with its top Te atoms (red spheres); the blue rectangles show the positions of the Se atoms on top of the Bi₂Te₃ film at the interface region with the Fe_xCu_{1-x}Se; the blue arrows show the positions in which the yellow Se atoms are located on top of the red Te atoms; (b) variation of the interfacial atomic column positions with respect to bulk Se and Te; the blue and red graphs correspond to the Se and Te atomic columns at the interface, respectively; the Se (blue) graph has been shifted up vertically for clarity; the values on the second *y*-axis correspond to the minimum and maximum displacement percentages with respect to the bulk average (*a*₀), respectively.

small amount as the position of the Se atoms change. Even up to 19% displacement of the Se with respect to the top Te positions only changes the bond energy by less than 20 meV. This is less than the corresponding energy for room temperature ($k_B T = 25.7$ meV). These results demonstrate that the bonding between Fe_xCu_{1-x}Se and Bi₂Te₃ has to be vdW-like, hence the experimentally observed ‘insensitivity’ of the atomic stacking registry at the interface.

In summary, we presented a structural study of single-crystalline Fe_xCu_{1-x}Se inclusions embedded in a Bi₂Te₃ film. Fe_xCu_{1-x}Se and Bi₂Te₃ are fully epitaxial despite different lattice symmetries and a lattice mismatch of 19%. Atomic-level structural and spectroscopic

studies carried out using aberration-corrected transmission electron microscopy revealed atomically sharp interfaces between the tetragonal phase of Fe_xCu_{1-x}Se and the Bi₂Te₃ thin film. The very large lattice mismatch at the Fe_xCu_{1-x}Se/Bi₂Te₃ interface does not lead to the formation of any network of misfit dislocations. First-principles energy calculations show that the formation of an abrupt and chemically ordered interface is realised through van der Waals-like bonding between the Se and Te atomic planes at the interface. This study shows that epitaxial heterostructures of materials with significant differences in lattice symmetry with corresponding large lattice mismatch can be realised through van der Waals bonding across the interface. This

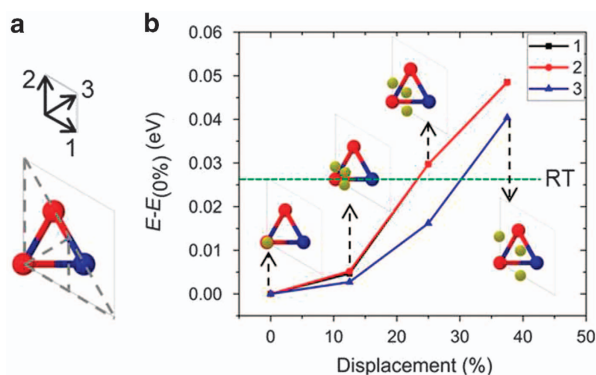


Figure 5 Energy calculations of Se atoms with respect to the bottom Te atomic position. (a) Top view image of the Bi₂Te₃ unit cell; the grey dashed lines show the positions of which 32 different sampling has been done for the Se bonding energy calculations; (b) relative energy variations along the three main crystallographic paths outlined in (a); the green dashed line shows the corresponding energy at room temperature (0.0257 eV).

study is of importance for the realisation of epitaxially stacked chalcogenide superconductor materials, i.e., CuSe, FeSe, Fe_xCu_{1-x}Se and 3D topological insulators.

CONFLICT OF INTEREST

The authors declare no conflict of interest.

ACKNOWLEDGEMENTS

SuperSTEM is the UK Engineering and Physical Sciences Research Council (EPSRC) National Facility for Aberration-Corrected STEM. All data created during this research are available by request from the University of York Data Catalogue <https://dx.doi.org/10.15124/5804ac81-b49b-46ce-aea8-73d47a9192cb>.

- 1 von Klitzing, K. Developments in the quantum hall effect. *Phil. Trans. R. Soc. A: Math. Phys. Eng. Sci.* **363**, 2203–2219 (2005).
- 2 Frank, F. C. & van der Merwe, J. H. One-dimensional dislocations. I. Static theory. *Proc. R. Soc. Lond. Series A. Math. Phys. Sci.* **198**, 205 (1949).
- 3 Frank, F. C. & van der Merwe, J. H. One-dimensional dislocations. II. Misfitting monolayers and oriented overgrowth. *Proc. R. Soc. Lond. Series A. Math. Phys. Sci.* **198**, 216 (1949).
- 4 Merwe, J. H. v. d. Equilibrium structure of a thin epitaxial film. *J. Appl. Phys.* **41**, 4725–4731 (1970).
- 5 Gourley, P. L. & Biefeld, R. M. Ga(As,P) strained-layer superlattices: a ternary semiconductor with independently adjustable band gap and lattice constant. *J. Vac. Sci. Tech.* **1**, 383–386 (1983).
- 6 Koma, A. Van der Waals epitaxy—a new epitaxial growth method for a highly lattice-mismatched system. *Thin Solid Films* **216**, 72–76 (1992).
- 7 Novoselov, K. S., Mishchenko, A., Carvalho, A. & Castro Neto, A. H. 2D materials and van der Waals heterostructures. *Science* **353**, 461–472 (2016).
- 8 Geim, A. K. & Grigorieva, I. V. Van der Waals heterostructures. *Nature* **499**, 419–425 (2013).
- 9 Shi, Y., Zhou, W., Lu, A.-Y., Fang, W., Lee, Y.-H., Hsu, A. L., Kim, S. M., Kim, K. K., Yang, H. Y., Li, L.-J., Idrobo, J.-C. & Kong, J. Van der Waals epitaxy of mos₂ layers using graphene as growth templates. *Nano Lett.* **12**, 2784–2791 (2012).
- 10 Liu, X., Smith, D. J., Fan, J., Zhang, Y.-H., Cao, H., Chen, Y. P., Leiner, J., Kirby, B. J., Dobrowolska, M. & Furdyna, J. K. Structural properties of Bi₂Te₃ and Bi₂Se₃ topological insulators grown by molecular beam epitaxy on GaAs(001) substrates. *Appl. Phys. Lett.* **99**, 171903 (2011).
- 11 Zhang, H., Liu, C.-X., Qi, X.-L., Dai, X., Fang, Z. & Zhang, S.-C. Topological insulators in Bi₂Se₃, Bi₂Te₃ and Sb₂Te₃ with a single dirac cone on the surface. *Nat. Phys.* **5**, 438–442 (2009).
- 12 Liu, H.-C., Li, H., He, Q. L., Sou, I. K., Goh, S. K. & Wang, J. Robust two-dimensional superconductivity and vortex system in Bi₂Te₃/FeTe heterostructures. *Sci. Rep.* **6**, 26168 (2016).
- 13 Xu, J.-P., Wang, M.-X., Liu, Z. L., Ge, J.-F., Yang, X., Liu, C., Xu, Z. A., Guan, D., Gao, C. L., Qian, D., Liu, Y., Wang, Q.-H., Zhang, F.-C., Xue, Q.-K. & Jia, J.-F. Experimental

detection of a majorana mode in the core of a magnetic vortex inside a topological insulator-superconductor Bi₂Te₃NbSe₂ heterostructure. *Phys. Rev. Lett.* **114**, 017001 (2015).

- 14 Qing Lin, H., Mingquan, H., Junying, S., Ying Hoi, L., Yi, L., Hongchao, L., Hongtao, H., Gan, W., Jiannong, W., Rolf, L. & Iam Keong, S. Anisotropic magnetic responses of a 2D-superconducting Bi₂Te₃/FeTe heterostructure. *J. Phys.: Cond. Matter* **27**, 345701 (2015).
- 15 He, Q. L., Liu, H., He, M., Lai, Y. H., He, H., Wang, G., Law, K. T., Lortz, R., Wang, J. & Sou, I. K. Two-dimensional superconductivity at the interface of a Bi₂Te₃/FeTe heterostructure. *Nat. Commun.* **5**, 4247 (2014).
- 16 Sochnikov, I., Bestwick, A. J., Williams, J. R., Lippman, T. M., Fisher, I. R., Goldhaber-Gordon, D., Kirtley, J. R. & Moler, K. A. Direct measurement of current-phase relations in superconductor/topological insulator/superconductor junctions. *Nano Lett.* **13**, 3086–3092 (2013).
- 17 Wang, M.-X., Liu, C., Xu, J.-P., Yang, F., Miao, L., Yao, M.-Y., Gao, C. L., Shen, C., Ma, X., Chen, X., Xu, Z.-A., Liu, Y., Zhang, S.-C., Qian, D., Jia, J.-F. & Xue, Q.-K. The coexistence of superconductivity and topological order in the Bi₂Se₃ thin films. *Science* **336**, 52–55 (2012).
- 18 Leijnse, M. & Flensberg, K. Introduction to topological superconductivity and majorana fermions. *Semicond. Sci. Tech.* **27**, 124003 (2012).
- 19 Nadj-Perge, S., Drozdov, I. K., Li, J., Chen, H., Jeon, S., Seo, J., MacDonald, A. H., Bernevig, B. A. & Yazdani, A. Observation of majorana fermions in ferromagnetic atomic chains on a superconductor. *Science* **346**, 602–607 (2014).
- 20 Zarepour, P., Hayat, A., Zhao, S. Y. F., Kreshchuk, M., Jain, A., Kwok, D. C., Lee, N., Cheong, S.-W., Xu, Z., Yang, A., Gu, G. D., Jia, S., Cava, R. J. & Burch, K. S. Proximity-induced high-temperature superconductivity in the topological insulators Bi₂Se₃ and Bi₂Te₃. *Nat. Commun.* **3**, 1056 (2012).
- 21 Mizukami, Y., Shishido, H., Shibauchi, T., Shimozawa, M., Yasumoto, S., Watanabe, D., Yamashita, M., Ikeda, H., Terashima, T., Kontani, H. & Matsuda, Y. Extremely strong-coupling superconductivity in artificial two-dimensional kondo lattices. *Nat. Phys.* **7**, 849–853 (2011).
- 22 Raveau, B. & Sarkar, T. Superconducting-like behaviour of the layered chalcogenides cus and cuse below 40 k. *Solid State Sci.* **13**, 1874–1878 (2011).
- 23 Harrison, S. E., Li, S., Huo, Y., Zhou, B., Chen, Y. L. & Harris, J. S. Two-step growth of high quality Bi₂Te₃ thin films on Al₂O₃ (0001) by molecular beam epitaxy. *Appl. Phys. Lett.* **102**, 171906 (2013).
- 24 Lucas, G., Burdet, P., Cantoni, M. & Hébert, C. Multivariate statistical analysis as a tool for the segmentation of 3D spectral data. *Micron* **52–53**, 49–56 (2013).
- 25 Clark, S. J., Segall, M. D., Pickard, C. J., Hasnip, P. J., Probert, M. I. J., Refson, K. & Payne, M. C. First principles methods using castep. *Crys. Mater.* **220**, 567 (2005).
- 26 Perdew, J. P., Burke, K. & Ernzerhof, M. Generalized gradient approximation made simple. *Phys. Rev. Lett.* **77**, 3865–3868 (1996).
- 27 Monkhorst, H. J. & Pack, J. D. Special points for brillouin-zone integrations. *Phys. Rev. B* **13**, 5188–5192 (1976).
- 28 McNellis, E. R., Meyer, J. & Reuter, K. Azobenzene at coinage metal surfaces: role of dispersive van der Waals interactions. *Phys. Rev. B* **80**, 205414 (2009).
- 29 Harrison, S. E., Collins-McIntyre, L. J., Schönherr, P., Vailionis, A., Srot, V., van Aken, P. A., Kellock, A. J., Pushp, A., Parkin, S. S. P., Harris, J. S., Zhou, B., Chen, Y. L. & Hesjedal, T. Massive Dirac fermion observed in lanthanide-doped topological insulator thin films. *Sci. Rep.* **5**, 15767 (2015).
- 30 Ghasemi, A., Kepaptsoglou, D., Figueroa, A. I., Naydenov, G. A., Hasnip, P. J., Probert, M. I. J., Ramasse, Q., Laan, G. v. d., Hesjedal, T. & Lazarov, V. K. Experimental and density functional study of mn doped Bi₂Te₃ topological insulator. *APL Mater.* **4**, 126103 (2016).
- 31 Zhang, J. M., Ming, W., Huang, Z., Liu, G. B., Kou, X., Fan, Y., Wang, K. L. & Yao, Y. Stability, electronic, and magnetic properties of the magnetically doped topological insulators Bi₂Se₃, Bi₂Te₃, and Sb₂Te₃. *Phys. Rev. B* **88**, 235131 (2013).
- 32 Shojaei, A. R., Vaez, A., Nourbakhsh, Z. & Madaniyan, Z. S. First-principles study of optical properties of α-cuse/klockmannite: bulk and nano-layers. *Thin Solid Films* **556**, 425–433 (2014).
- 33 Shojaei, A. R. Electrical conductivity plus probability of superconductivity in α-cuse/klockmannite: bulk and nano-layers. *J. Alloys Comp.* **632**, 568–574 (2015).



This work is licensed under a Creative Commons Attribution 4.0 International License. The images or other third party material in this article are included in the article's Creative Commons license, unless indicated otherwise in the credit line; if the material is not included under the Creative Commons license, users will need to obtain permission from the license holder to reproduce the material. To view a copy of this license, visit <http://creativecommons.org/licenses/by/4.0/>

© The Author(s) 2017